



Sliding wear behavior of cold metal transfer clad Stellite 12 hardfacings on martensitic stainless steel

Jaakko Tapiola¹ · Jari Tuominen¹ · Jorma Vihinen² · Petri Vuoristo¹

Received: 24 May 2022 / Accepted: 23 September 2022
© The Author(s) 2022

Abstract

Cold metal transfer (CMT) welding technique was used in the manufacturing of hypoeutectic carbide-type Co-based Stellite 12 hardfacings on martensitic stainless steel. It was discovered that the CMT process is capable of producing relatively thick (> 2.5 mm) low diluted single-layer coatings with cored Stellite 12 wire without cracks and pores. These coatings were investigated using microscopy (optical and scanning electron microscopy), X-ray diffraction, and hardness measurements. The high melting point chromium and tungsten particles inside the cored wire were relatively large and therefore remained unmelted in the clad layers. Self-mated sliding wear tests were performed using a pin-on-disc tribometer at room temperature and at 300 °C to determine the wear resistance and friction of the coatings. The coefficients of friction were relatively similar (~0.35) at both temperatures. Differences were exhibited in the ~40% greater loss of material at high temperature. The wear performance of the CMT clad Stellite 12 coatings did not, however, reach the wear performance of self-mated laser clad Stellite 6 reference material. CMT hardfacing was finally successfully demonstrated on a ring-shaped component.

Keywords Cold metal transfer · CMT · Overlay welding · Hardfacing · Stellite, sliding wear

1 Introduction

Surface treatment or coating of materials is carried out in order to improve their lifetime by enhancing properties like corrosion and wear resistance via a durable layer or multiple layers added onto the surface. Typical methods include thermal spraying, laser cladding, overlay welding, electrochemical methods, and physical and chemical vapor deposition for example [1, 2]. One rather new method in the area of overlay welding is cold metal transfer (CMT). It was originally developed for dissimilar metal welding, especially for the joining of aluminum and steel [3, 4]. Because of the low heat input of the process, it can also adapt to the needs of overlay welding, capable of producing low diluted coatings with a limited heat load into the substrate.

Usually, the problem with traditional arc welding/cladding methods is the high amount of heat they transfer to the

substrate during the process. Heat alters the microstructure and phase composition of the material, which is not desirable, because of the possible changes in critical material properties. Excessive heat makes also controlling dilution difficult, distorts the components, or causes high residual stresses. Another issue with conventional arc welding methods is the spattering of the filler material. This spatter around the weld usually needs to be cleaned, which consumes economical resources and time. CMT exploits a technique developed by Fronius International GmbH, where the rapid back and forth movement of the filler wire reduces heat input into the substrate, and simultaneously, it assists the mechanical, low current transfer of the filler material [5]. CMT has been applied in overlay welding mostly with different nickel-base and aluminum [3, 6–12] solid wires, and recently, a study about CMT cladding of Co-based Stellite 21 hardfacing on tool steel [13] was also published.

Co-based hardfacing alloys are versatile alloys exhibiting such properties as high-temperature hardness, corrosion, galling, and sliding wear resistance, which makes these alloys suitable for applications that suffer from hard operational conditions. Depending on the chemical composition, they are subdivided into solid solution strengthened, carbide, and intermetallic-type alloys. Solid solution strengthened

✉ Jari Tuominen
jari.tuominen@tuni.fi

¹ Materials Science and Environmental Engineering, Tampere University, 33720 Tampere, Finland

² Automation Technology and Mechanical Engineering, Tampere University, 33720 Tampere, Finland

and carbide-type alloys are known as Stellites, and intermetallic alloys are called Triballoys [14]. Some of these alloys harden during machining depending on the alloying elements. The phase transformation for work hardening takes place via the change in the crystal structure of Co (face-centered cubic γ -Co to hexagonal close-packed ϵ -Co). This transformation occurs at 417 °C if cobalt is cooled extremely slowly. Usually, the fcc structure is retained at RT because of the nature of the transformation, and hcp transformation is only caused by mechanical stress or time at high temperatures. The low stacking fault energy (SFE) of the unstable fcc structure leads to material properties like high yield strength and high work-hardening rate and makes the material less predisposed to fatigue under cyclic stress. These attributes lead to the material capable of preventing damage during sliding wear and are the reasons behind the resistance to erosion-corrosion and cavitation of cobalt as well [14, 15].

Stellites are also non-magnetic alloys that can be tailored for specific applications involving, for instance, unlubricated systems and elevated temperatures. Alloying elements including Cr, Mo, W, and Si favor the phase transformation and work hardening by deducting the SFE of the Co matrix, whereas elements such as Fe, Ni, and Mn stabilize the metastable fcc structure by promoting SFE [16, 17]. Besides affecting SFE, Cr, Mo, and W are carbide formers forming complex carbides (MC , M_6C , M_7C_3 and $M_{23}C_6$) in CoCr matrix. Most of the W and Mo remain, however, in the solid solution hindering the movements of dislocations and slips due to their large atomic size. They are also known to form intermetallic phases like $Co_3(Mo, W)$. In carbide-type Stellites, carbon content controls the carbide volume and hardness. They can be grouped into hypo- and hypereutectic alloys by carbon content [18, 19].

The most common methods in the manufacturing of Stellite coatings that exploit the Stellite feedstock material in powder form are laser and plasma-transferred arc (PTA) cladding. Tungsten inert gas (TIG) and metal inert gas (MIG) welding are also commonly used techniques, and they exploit the feedstock material in the shape of wire or rod. Some studies with different coating techniques are reviewed below. Yaedu et al. [20] applied PTA hardfacing with Stellite 1 on different steels and studied the effects of dilution and substrate on the hardness and wear rates of the coatings. They concluded that lower dilution deposits are typically harder and exhibit lower wear rates. In addition, the substrate with the highest carbon content exhibited the best properties in terms of lower dilution levels and lower wear rates. Frenk et al. [21] studied the microstructural effects on the sliding wear resistance of a laser-cladded Co-based hypoeutectic Stellite 6 alloy in powder form. Different laser processing conditions were used to investigate the differences in microstructures when the manufacturing methods were either fast or slow, which

affects greatly the cooling rates and thus the refinement of the structures. They concluded that SFE is the main factor affecting the wear behavior. The lower the SFE, the better the results. Dilution should be minimized to maximize the wear resistance of the laser-cladded Stellite 6 coatings.

Fouilland et al. [22] studied the friction behavior of MIG welded Stellite 21 hardfacings and friction-induced work hardening of the multilayer coatings. Hardfacings were deposited on hot work tool steel preheated to 400 °C. The feedstock wire was flux-cored Stellite 21 1.6 mm in diameter. Four-layer hardfacings were produced to eliminate the excessive dilution. They observed that the highest work hardening was achieved with the lowest dilution increasing the wear performance of clad layers.

In another study by Fouilland et al. [23] microstructural changes in Stellite 21 caused by different welding energies were studied. It was found out that welding energy had a great influence on the secondary precipitation, which occurs in preceding layers during deposition of successive layers. With higher welding energy, fine cuboids of $Cr_{23}C_6$ precipitated even in the cobalt dendrites.

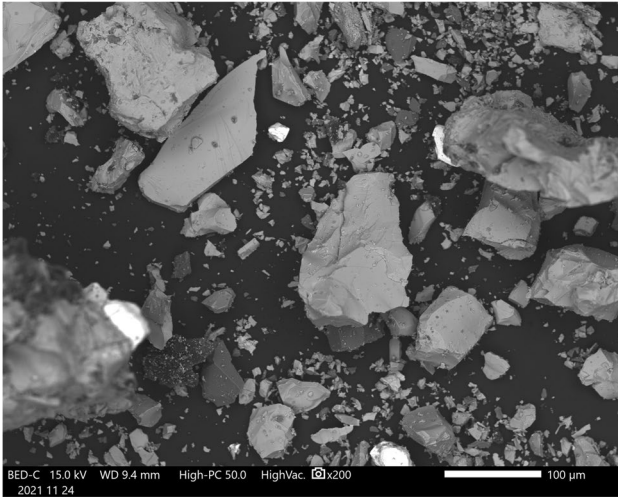
Motallebzadeh et al. [24] studied the sliding wear characteristics of PTA-deposited Stellite 12 and Stellite 12 with a 10wt.% Mo addition at elevated temperatures. Both of the materials, Stellite 12 and Mo were used in the powder form. Five-millimeter-thick clads were deposited and ground to a thickness of 2.5 mm. They noticed that Mo addition not only increased the hardness of the clad but also enhanced the wear resistance at all temperatures. The average hardness of Stellite 12 deposits was ~490 HV while the coating with Mo-addition had the hardness of ~620 HV. Coefficient of friction (COF) values was also slightly decreased with the Mo-addition. The relative wear rates were significantly reduced in the clads with Mo-addition.

Rajeev et al. [13] exploited CMT in depositing Stellite 21 on AISI H13 tool steel. Their goal was to study the deposition of wear-resistant material to a known die material used in forging to lengthen the service life of the component in question. They also exhibited hardfacing to a preheated substrate and found out that preheating made the heat-affected zone (HAZ) less susceptible to cracking. The cracking in the HAZ is due to the formation of brittle martensite upon rapid cooling. They were able to produce low diluted (3–4%) Stellite 21 coatings and crack-free coatings using annealed H13 with 400 °C preheating.

The objective of this study was to optimize CMT process parameters for a cored Stellite 12 wire and test the coatings manufactured for their wear properties using a pin-on-disc tribometer. This research area has not yet been studied profoundly, especially with cored wires using an advanced MIG/MAG process called the CMT. A relatively inexpensive CMT process with high productivity and material

Table 1 Chemical compositions of St12 cored wire and X20Cr13 substrate in wt.% according to analysis certificates

| Material | C | Mn | Si | Fe | Cr | W | Ni | Co | P | S |
|----------|------|------|------|------|-------|-----|------|-----|------|--------|
| St12 | 1.4 | 1.0 | 1.5 | <2.5 | 29.5 | 8.5 | <3.0 | Bal | | |
| X20Cr13 | 0.18 | 0.59 | 0.41 | Bal | 12.68 | | | | 0.02 | 0.0018 |

**Fig. 1** Backscattered SEM image of the powder inside the cored St12 wire. The largest particles are chromium and the brightest ones are tungsten

efficiency could offer a cost-efficient alternative for laser and PTA cladding in hardfacing.

2 Materials and methods

2.1 Materials

The filler material used was a Stellite 12 (St12) cored wire (Thalit 12G, Corodur Verschleiss-Schutz GmbH, Thale, Germany) 1.2 mm in diameter. St12 is a carbide-type hypoeutectic Co-based hardfacing alloy with moderate hardness provided by carbon and carbide formers. This alloy has claimed to have excellent resistance to abrasion, erosion, cavitation, and severe sliding wear, and it can be used in applications reaching up to 700 °C [25]. Its chemical composition is presented in Table 1. Besides the elements reported in the analysis certificate, the filler inside the wire contained some Al, F, Na, Ca, and K particles, which are effective arc stabilizers and deoxidizers [26]. Angular Cr and W particles found inside the wire were up to 250 and 120 μm in size, respectively. Representative filler inside the wire is displayed in Fig. 1. Sheath thickness was 0.15 mm, and the type of joint was lapped. The substrate was a martensitic stainless steel X20Cr13 as discs with 100 mm diameter and thickness of 30 mm. It was in QT800 condition, meaning it was hardened

Table 2 Optimized CMT cladding/hardfacing parameters for St12 cored wire on X20Cr13 steel

| Parameter | Value |
|------------------------------------|-----------|
| Voltage (V_{ave}) | 14.7 V |
| Current (A_{ave}) | 169 A |
| Arc power (W_{ave}) | 2484 W |
| Travel speed (TS) | 3 mm/s |
| Wire feed rate (WFR) | 6.5 m/min |
| Process gas (Ar+2CO ₂) | 15 l/min |
| Weaving width | 16 mm |
| Preheat | None |

and tempered as follows: annealing at 950 °C for 150 min and quenching in oil followed by tempering at 650 °C for 300 min and cooled in air. The chemical composition of the X20Cr13 substrate is presented in Table 1.

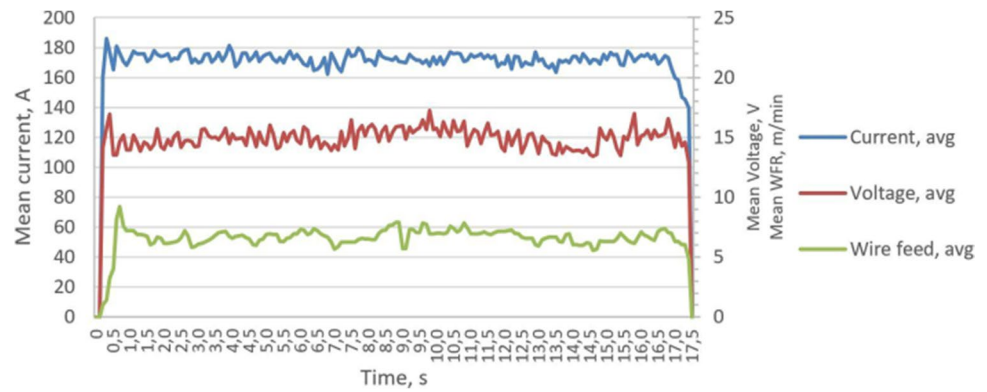
2.2 Cladding/hardfacing

Cladding experiments were conducted with a Fronius CMT Advanced 4000R single-wire welding equipment (Fronius International GmbH, Wels, Austria) mounted to an ABB IRB 4600–40/2.55 robot with an ABB IRBPA-750 turntable (ABB, Västerås, Sweden). After a large series of cladding experiments to produce low-diluted fusion-bonded single-layer clads without pores and cracks, the optimized cladding parameters are presented in Table 2. Fronius Xplorer software was used during the cladding to collect more information about the welding process. It collects process data with 10 Hz sampling rate, which is a slower rate than the frequency of CMT cycles and is not therefore comparable to higher sampling rate oscilloscope measurements. The graphs of these process parameters are shown in Fig. 2. Although the wire feed rate (WFR) seems to vary vastly, the mean value calculated from this data was 6.5 m/min, which was the pre-set value. This exhibits how the process is adapting all the time during cladding. It is also seen from the graphs that the starting current was set higher and the final current lower than the working parameters.

2.3 Characterization

Both optical and scanning electron microscopy (OM and SEM) were used in inspecting the sample cross-sections prepared from the clad beads. Picral reagent was used as

Fig. 2 CMT process parameters during cladding of St12 as a function of time



an etchant to bring out the microstructure of the clad and HAZ in steel. The optical microscope used was a Leica DM 2500 M (Leica Microsystems GmbH, Wetzlar, Germany), and the SEMs were a Philips XL-30 (Philips, Amsterdam, the Netherlands) and JEOL JSM-IT500 (Jeol Ltd., Tokyo, Japan) both with the energy-dispersive X-ray spectroscopy (EDS). Hardness measurements were conducted using a Matsuzawa MMT-XT (Matsuzawa Co Ltd, Akita, Japan) Vickers microhardness tester. To reveal crystal structures and phases present in clads, an X-ray diffractometer, Panalytical Empyrean Multipurpose Diffractometer (Malvern Panalytical Ltd, Malvern, UK), was employed using the $\text{CuK}\alpha$ radiation at the voltage of 45 kV and the current of 40 mA. The scanning angle 2θ covered a range of $20\text{--}80^\circ$.

Geometrical dilution was calculated from the cross-section perpendicular to cladding direction using the equation:

$$\text{Dilution} = \frac{A_m}{A_c + A_m} \times 100\% \quad (1)$$

where A_m is the cross-sectional area of melted material below the substrate surface and A_c melted material above the substrate surface.

2.4 Tribology

Self-mated sliding wear tests for the parameter optimized specimens were run to determine their wear behavior under different temperatures and to define the COFs. Wear tests were conducted with a pin-on-disc device CETR UMT-2 (Center for Tribology, Campbell, USA). For the wear tests, multiple discs were clad with St12, machined to specific dimensions, and test surfaces ground to a R_a of $0.3\text{--}0.4\ \mu\text{m}$. The size of the disc was 70 mm in diameter and 10 mm in thickness. The pins were removed from the clad by wire cutting. The diameter of the flat pin was 6.35 mm. Figure 3 shows the schematic presentation of the test. Before each test, the wear surfaces of both the disc and the pin were cleaned with ethanol. The weighing was

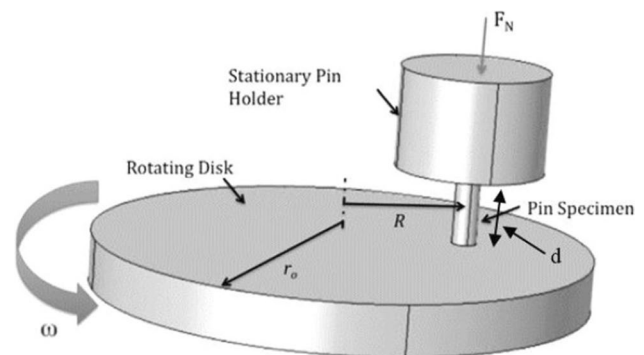


Fig. 3 Schematic presentation of a pin-on-disc test setup (edited from the Ref. [35])

done with a TEOPAL scale (accuracy 0.001 g). The test pieces were weighed five times before and after the test, and the average was calculated.

The wear tests were performed in dry conditions at RT and $300\ ^\circ\text{C}$ in an air atmosphere using the normal load of 150 N, which gave the nominal contact pressure of 4.7 MPa, the sliding speed of 2400 mm/min, and the testing time of 6 h. Repeatability and the accuracy of this test can be evaluated with a coefficient of variation (COV). With the used specimen geometry and the test parameters, COVs for mass loss and COF were 9.0% and 5.8% at RT and 12.6% and 5.6% at $300\ ^\circ\text{C}$. According to Ref. [27], COV of 20% or less for mass loss is a sign of properly conducted tests. The worn track on the disc and the worn surface of the pin were examined with SEM. Multi-layered Stellite 6 with negligible dilution manufactured by the industrial laser cladding workshop by the coaxial powder laser cladding process was used as reference material in the tests. Stellite 6 is a widely used hardfacing alloy in the industrial laser cladding combining good corrosion and wear properties, a fair compromise between hardness and toughness as well as good weldability without the need to use preheating.

3 Results and discussion

3.1 Microstructure

The OM image of the single bead manufactured with optimized process parameters is illustrated in Fig. 4. The maximum height of the bead is 2.4 mm, width 19.3 mm with a geometrical dilution of 1.7%, and approximately 3.0 kg/h deposition rate as calculated from the bead dimensions. The maximum depth of the crack-free HAZ is ~1.6 mm. Even though the dilution is remarkably low, there still is a fusion bond between the clad layer and the substrate. Contact angles at both sides of beads are small enough ($<40^\circ$) to enable defect-free overlapping of adjacent beads when fabricating continuous coating layers as will be shown in Sect. 3.4. Spherical dots poorly seen in the low magnification cross-section are unmelted powder particles inside the cored wire as will be explained and shown below.

The clad specimens were further examined with SEM, and some interesting sites were analyzed for their composition with EDS. The composition of the unmelted particles was one of these interests. The white particles in Fig. 5a are 100 wt.% tungsten, and the smaller black particles are

100 wt.% chromium. Tungsten particles are profoundly concentrated on the lower part of the clad without disturbing the fusion line. They have sunk to the bottom of the melt due to higher density than the cobalt alloy ($\rho = 19.3 \text{ g/cm}^3$ for W vs. $\rho = 8.53 \text{ g/cm}^3$ for St12). According to image analysis, unmelted W content in the clad was ~1.7 vol.% averaging ~70 μm in diameter. The amount of unmelted Cr particles was far less than W particles, and they were distributed more homogeneously across the clad cross-section. EDS point analyses were also taken from the dendritic and interdendritic zones to see how the elements solidify and segregate. The results of these single-point analyses taken from the one region of the bead from the locations pointed by arrows in Fig. 5b are presented in Table 3. The tungsten content within all areas is rather low, as some amount of it remains unmelted after the welding process. The chromium is higher in the interdendritic zone, whereas the cobalt content is higher in the dendrites. Although carbon is a problematic element for EDS and its quantity cannot be accurately measured, the results indicated that the carbon tends to locate in the interdendritic zone; the carbon peaks are higher there than in the dendritic zones indicating the formation of carbides with chromium and tungsten. Therefore,

Fig. 4 Low-magnification OM image of single bead of St12 on X20Cr13 CMT clad with optimized parameters

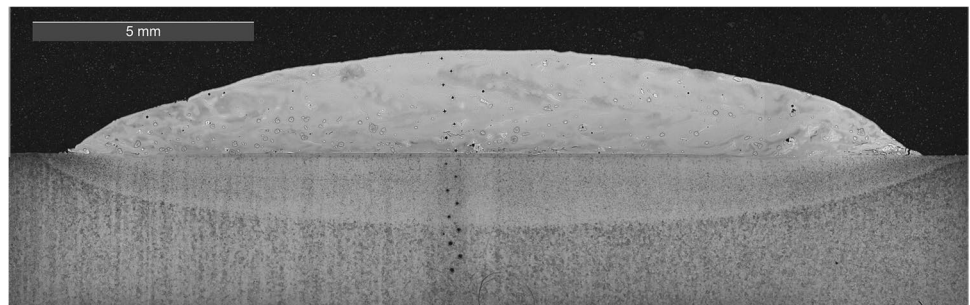


Fig. 5 High magnification backscattered electron (BSE) SEM images of St12 fabricated with CMT: **a** unmelted particles and **b** hypoeutectic structure with dendritic and interdendritic regions

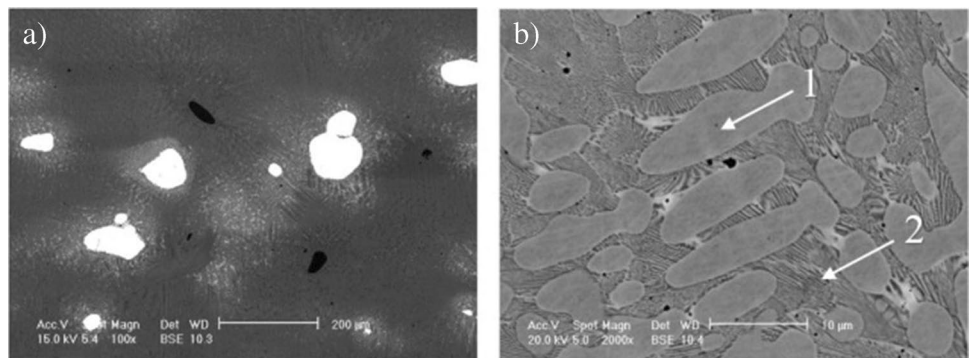


Table 3 Results of EDS point analyses in wt.%

| Location | Al | Si | Cr | Mn | Fe | Co | W |
|----------|-----|-----|------|-----|-----|------|-----|
| Point 1 | 0.3 | 1.2 | 21.6 | 0.7 | 8.2 | 64.1 | 3.9 |
| Point 2 | 0.2 | 1.4 | 33.5 | 1.0 | 7.2 | 52.0 | 4.7 |

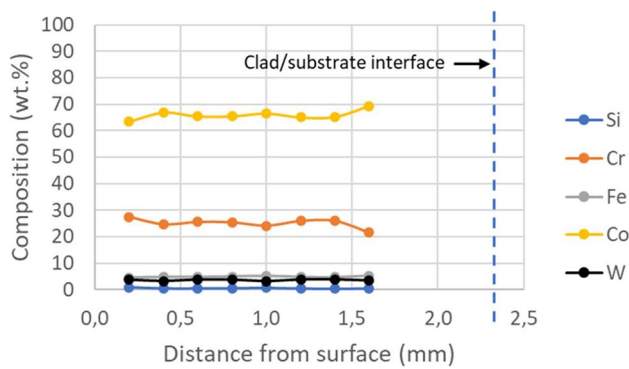


Fig. 6 EDS composition profile through the depth of St12 on X20Cr13

the interdendritic region is concluded to consist of a lamellar mixture of the solid solution and eutectic carbides, a well-known structure of hypoeutectic Stellite alloy. Some tiny black dots seen in the interdendritic regions in Fig. 5b are aluminum oxides with traces of Ca, K, F, and Na. According to image analysis, interdendritic regions occupy ~41 vol.% of the clad, which is in good agreement with Ref. [24].

The chemical composition throughout the coating was obtained with an EDS area analysis. The analyzed areas were 43 μm in diameter, and they were taken at 200- μm intervals as shown in Fig. 6. The average iron concentration is 4.9 wt.% in the clad which indicates very low chemical dilution and confirms the results of low geometrical dilution reported above. Intermixed Fe is also homogeneously distributed across the cross-section, which indicates good corrosion performance. The amount of tungsten (~3.6 wt.%) and chromium (~25.1 wt.%) in the matrix is lower, particularly in the case of tungsten, than the values given in the material certificate (Table 1) as the particles remained unmelted and did not dissolve in the melt pool during the cladding process.

The primary (λ_1) and secondary dendrite arm spacings (λ_2) were measured from different depths of the clad. On top of the clad, λ_1 and λ_2 ranged from 8 to 14 μm and from 3 to 4 μm , at the depth of ~0.6 mm from 6 to 15 and from 3 to 4 μm , and at the depth of ~1.3 mm from 13 to 18 μm and from 4 to 6 μm indicating very high solidification and cooling rates. The primary and secondary dendrite arm spacings were reported to be in laser clad St6 9.1 ± 2.1 and 1.5–3.0 μm with theoretical welding energy of 0.10 kJ/mm [21]. In another study, primary dendrite arm spacings for St6 clad with MMA (0.92 kJ/mm), TIG (0.66 kJ/mm), and laser (0.24 kJ/mm) were reported to be 14–20 μm , 10–18 μm , and 8–13 μm , respectively [15, 28]. These results suggest that arc power used in this study was not perhaps high enough to maintain the melt pool across the whole weaving width. Otherwise, the relatively high welding energy (~0.83 kJ/

mm) used in this study supposed to have led to much coarser structure. Variations of these dendrite arm spacings as a function of welding energy (kJ/mm) are illustrated in Fig. 7. Drop in primary dendrite arm spacing (λ_1) is clearly seen at the location of ~0.83 kJ/mm. On the other hand, when considering specific energy (J/mm^2) instead of line welding energy (kJ/mm), arm spacing values make better sense. Specific energy used in this study was 43 J/mm^2 , which is at the same level as in referenced laser clad Stellites (48 and 52 J/mm^2) [21, 28]. Specific energies given for laser clad Stellites are theoretical values. Poor process energy efficiency in these CO_2 laser clad specimens was not taken into account. In any case, finer grain structure is known to be beneficial providing higher matrix hardness via grain boundary strengthening as was shown in Ref. [15] giving clear benefit for the low heat input cladding methods such as laser and CMT. The rate of strain hardening is also known to increase as the microstructure becomes refined [28].

The CMT clad Stellite 12 was also analyzed with XRD to identify the phase compositions. The representative XRD curve taken from the surface of the machined wear specimen is illustrated in Fig. 8. The peaks that could be identified were cubic γ -Co (fcc) solid solution, hexagonal close-packed ϵ -Co (hcp), and orthorhombic or hexagonal M_7C_3 carbide ($\text{M} = \text{Cr}, \text{Co}, \text{Fe}, \text{W}$). According to Hou et al. [29], M_7C_3 carbides found from PTA clad St12 are hexagonal as proved by the TEM studies. Hexagonal cobalt may have formed during the machining of the sample surface.

To summarize the microstructural analysis, the process parameter optimization led to a low diluted, fusion bonded, and defect-free hardfacing. There is a relatively high amount of unmelted high melting point Cr (T_m 1907 $^\circ\text{C}$) and W (T_m 3422 $^\circ\text{C}$) particles left at the bottom half of the clad layer, which could not be melted without causing excessive dilution to the clad layer. The size of these rather coarse particles inside the cored wire designed for the conventional MIG/

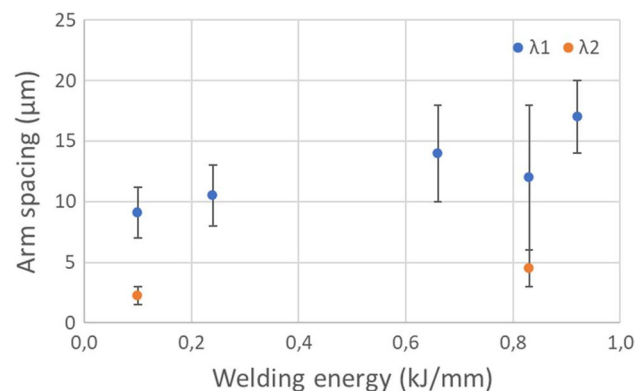
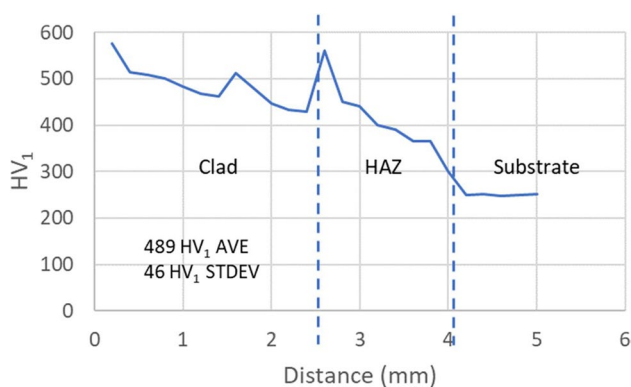
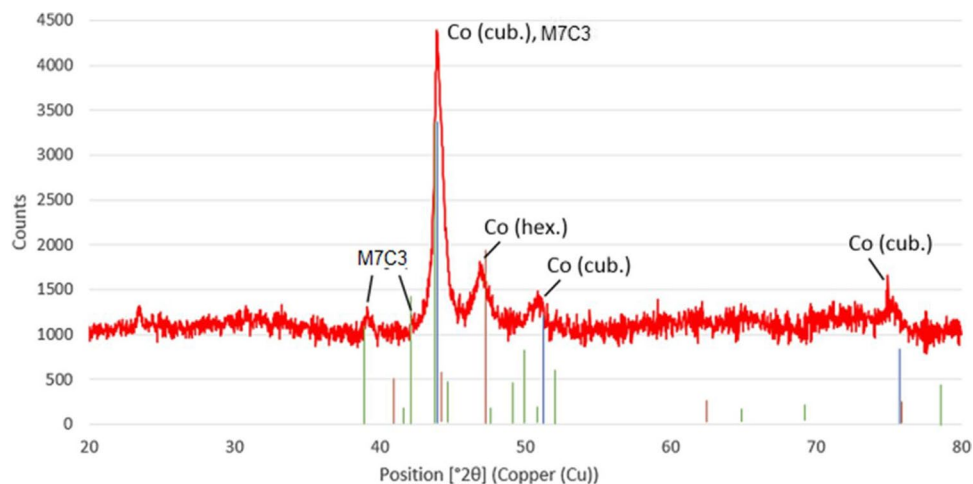


Fig. 7 Variations in the dendrite arm spacing as a function of welding energy (kJ/mm) [15, 21, 28]

Fig. 8 XRD pattern of St12 on X20Cr13**Fig. 9** Hardness profile of St12 on X20Cr13 manufactured with CMT

MAG process should be decreased to make hardfacing more homogenous by the CMT process.

3.2 Microhardness

Hardness measurements were performed to study the mechanical properties of the clad. The values should be between 450 and 550HV₁ according to the manufacturer of the wire. If the hardness is less than this, it is an indication of excessive dilution occurred in the overlay welding process. Microhardness profile is presented in Fig. 9. The average microhardness of the clad is 489HV₁, which is rather low taking into account the low dilution. It is, however, similar to hardness reported for PTA clad St12 in Ref. [24] and higher than 429HV reported for PTA clad St12 with dilution of 8.5% [29]. Low microhardness is attributed to the unmelted W and Cr particles because they do not participate in forming carbides and providing solid solution strengthening. W and Cr are also important elements in diminishing the SFE and promoting the work hardening and related γ -Co (fcc) \rightarrow ϵ -Co (hcp) phase transformation, which may compromise the wear resistance by reducing the matrix's ability

Table 4 Average microhardness values HV₁ and STDEV (in parentheses) measured from the non-tested and tested surfaces (average of four measurements)

| | Non-tested | RT | Increase (%) | 300 °C | Increase (%) |
|-----------|------------|----------|--------------|----------|--------------|
| St12 disc | 643 (35) | 738 (43) | 14.8 | 770 (62) | 19.8 |
| St12 pin | 451 (11) | 712 (40) | 57.9 | 783 (39) | 73.6 |
| St6 disc | 561 (30) | 625 (49) | 11.4 | 775 (34) | 38.2 |
| St 6 pin | 672 (26) | 692 (76) | 3.0 | 852 (36) | 26.8 |

to work harden. The microhardness of the unmelted W and Cr was 517HV_{0.05} (39 STDEV) and 230HV_{0.05} (12 STDEV), respectively, both softer than the surrounding cobalt matrix (~530HV_{0.05}). HV_{0.05} was used instead of HV₁ to fit the indentation to the unmelted particles. It can be also seen that HAZ exhibited significant increase in hardness near the fusion line more than doubling the hardness of the substrate due to formation of martensite during cooling.

Hardness measurements were also taken from the surfaces of ground discs and pins before subjecting them to wear tests. Values indicate strong work hardening due to machining operations as shown in Table 4.

3.3 Wear tests

The sliding wear test results for CMT clad St12 expressed as mass losses are shown in Fig. 10a. The total mass loss increased by 37% when the temperature was elevated from RT to 300 °C. The mass loss of the pin was reduced by half, while the mass loss of the disc was nearly doubled. This could be attributed to the strong adherence and material transfer from the disc to the pin in the test at 300 °C. It was also noted that the surface hardness of the pin increased more at 300 °C compared to RT due to strain hardening (Table 4). Hardness growths in the pin at 300 °C and RT were 74% and 58%, respectively. These strain hardening

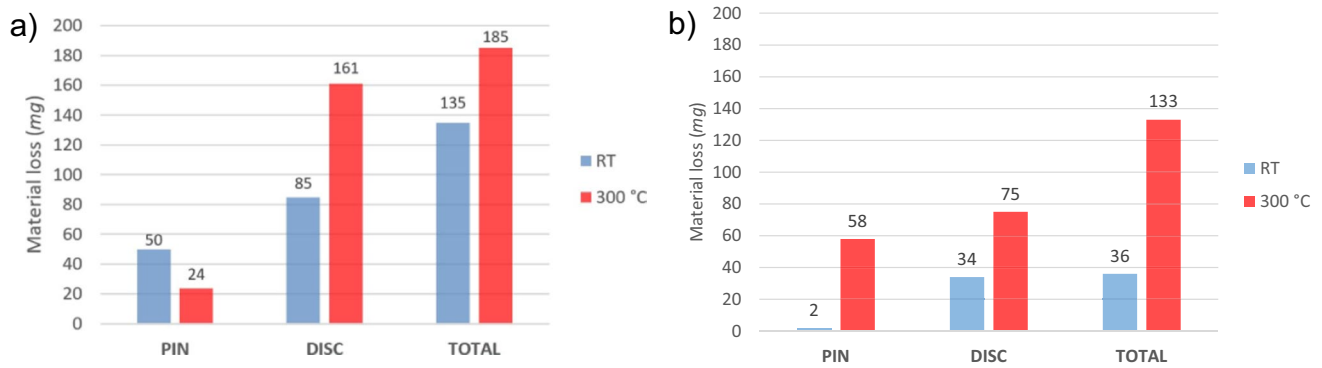


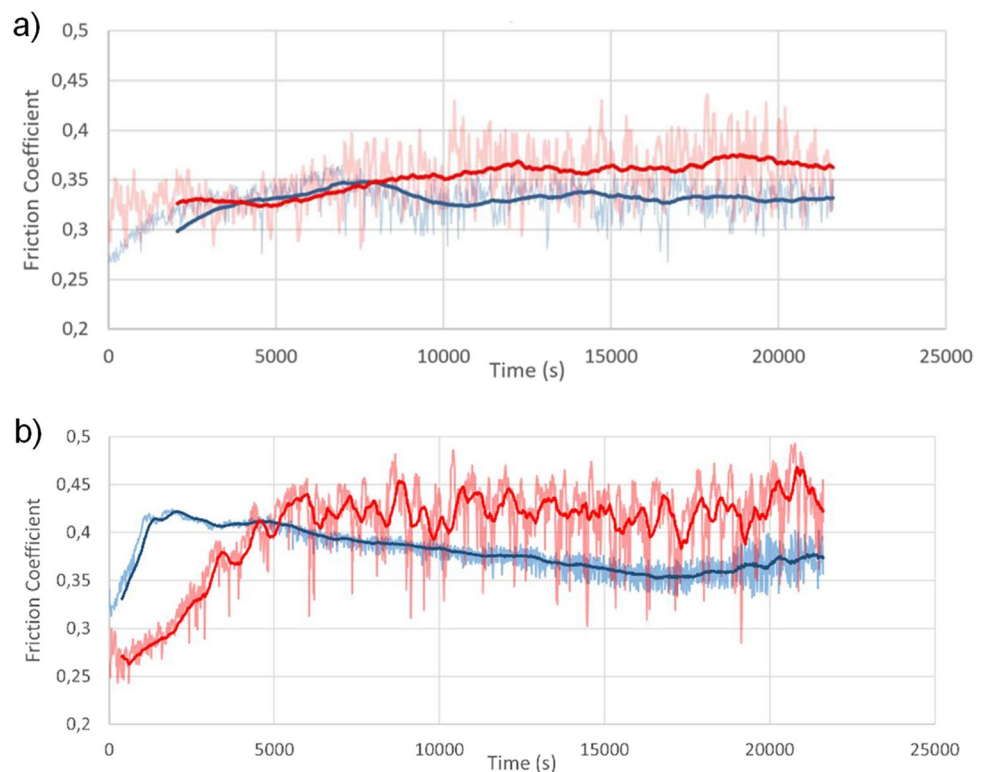
Fig. 10 Sliding wear test results at RT and 300 °C for the self-mated **a** St12 hardfaced with CMT cladding and **b** St6 hardfaced with laser cladding

rates are rather impressive taking into account that not all the W and Cr, which favor γ -Co (fcc) to ϵ -Co (hcp) transformation, were dissolved in the solid solution. As displayed in Fig. 10b, the total mass loss values for the reference material Stellite 6 hardfaced with laser cladding were 36 mg at RT and 133 mg at 300 °C exhibiting significantly higher wear resistance than CMT hardfaced St12, particularly at RT. At elevated temperature, the total mass loss increased much more (269%) than in CMT clad St12 probably due to higher thermal softening. According to Refs. [30, 31], hardness values of St12 and St6 at 300 °C are 390 and 345HV, respectively. In principle, St6 is supposed to be a softer and

less wear-resistant alloy than the grade St12 emphasizing the role of microstructural refinement and full participation of all the alloying elements. Even if not any microstructural analysis was conducted for the reference material in this study, the superiority in sliding wear resistance could be attributed to these factors.

The COF values for CMT clad St12 as a function of test time are presented in Fig. 11a. The COF at RT is somewhat lower than the COF at 300 °C. Both values are around 0.35. This result is against the findings reported in Refs. [24, 32], where St12 was tested against alumina ball and CrMo-steel at RT and elevated temperatures. COF values

Fig. 11 COF values as a function of time for self-mated **a** CMT clad St12 and **b** laser clad St6 at RT (blue) and 300 °C (red)



typically decrease at elevated temperatures due to lower shear strengths and formation of low-friction oxide layers. No reference data about the friction behavior was found for the self-mated Stellite alloy tests in dry conditions. COF values for the self-mated Stellite 6 produced by laser cladding were around 0.4 as shown in Fig. 11b.

3.3.1 Wear scars at RT

A closer inspection of wear tracks with SEM and EDS revealed that thick oxidized layer of transferred metal from the counterpart formed particularly on top of unmelted tungsten particles on the wear track (the spots marked with number 1 and pointed by white arrows in Fig. 12a). Both the disc and the pin exhibited this behavior at RT. COF of metallic tungsten is not known, but according to Ellingham diagrams, its tendency to form oxides lies between cobalt and chromium [33, 34]. Dark particle on the ground surface (marked with number 2) was identified as 100 wt.% chromium and bright particle (marked with number 3) as 100 wt.% tungsten. The amount of Fe was also measured from the ground surfaces of pin and disc. The highest reading was 5.6 wt.% indicating negligible dilution. White rectangular area on the surface of disc in Fig. 12a spots the EDS analysis area and Fig. 12b the sampling area.

Fig. 12 Top view of the tested disc at RT: **a** BSE SEM micrograph showing the characteristic morphologies of non-tested ground surface and the wear scar of St12 on top of the disc and **b** sketch showing the sampling area

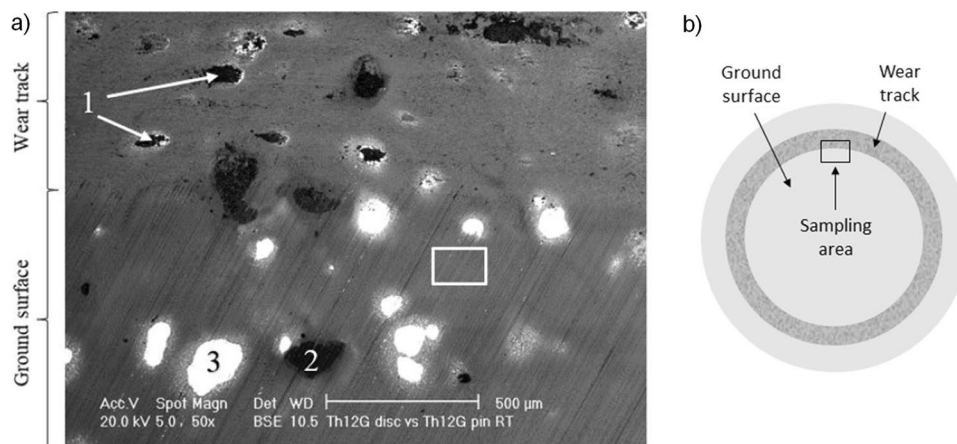
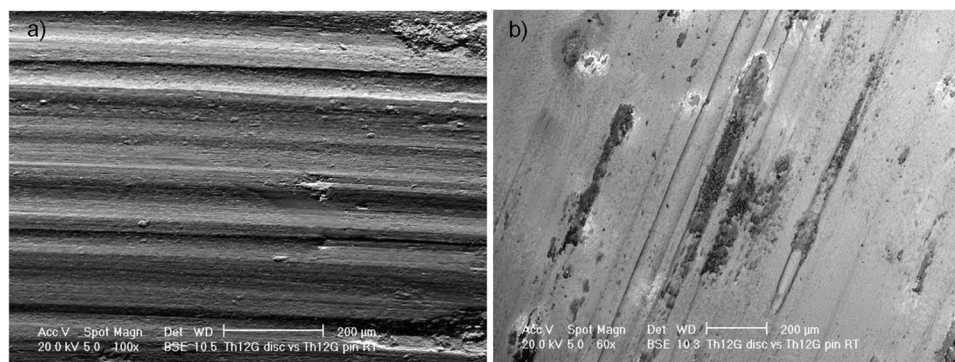


Fig. 13 BSE SEM images taken from the wear scars of **a** St12 disc and **b** St12 pin after the test at RT



A higher magnification image shown in Fig. 13a taken from the wear scar of St12 disc reveals distinctive, continuous, and smooth grooves on the wear track. The grooves are $\sim 50\text{--}60\ \mu\text{m}$ in width much wider than the mean free path between eutectic ($\sim 9\ \mu\text{m}$). If assuming that grooves were created by strain hardened and oxidized wear debris (3-body abrasion) and/or unmelted tungsten particles (2-body abrasion), such a short mean free path between the carbide-rich regions should have given effective protection against larger abrasives. Material which was originally within the grooves was, however, neatly cut away by micro-cutting indicating limited wear performance. Another finding was that there were not clear signs of plastic deformation on the surfaces or oxide layers in the other regions of wear scar. The wear scar on the pin was similar to one on the disc, except for longer elongating oxide layers originating from the top of unmelted tungsten particles as shown in Fig. 13b. Some deeper grooves were also visible, but no signs of plastic deformation were detected. Therefore, the wear mechanisms can be assumed to be similar to that in the disc.

3.3.2 Wear scars at 300 °C

Similarly as in the disc after the test at RT, SEM images of the St12 disc surface revealed an oxide layer of adhered

Co-alloy on top of unmelted tungsten particles in the wear track (spot 2) in Fig. 14. The difference to RT is the higher amount of oxidized wear debris adhered on the wear track, identified with number 3 in Fig. 14. At elevated temperature, a higher amount of Co-alloy seems to have transferred from the pin to the disc than at RT. These regions show also signs of plastic deformation as a result of thermal softening. A white particle off the wear track was analyzed with EDS and identified as 100 wt.% tungsten.

A higher magnification image of the wear track in the disc reveals some differences between the wear behavior at

elevated temperature and RT. At RT (Fig. 13a), the grooves were more distinguishable, while the grooves in Fig. 15a are clearly more indistinct with signs of plastic deformation and adhered wear debris. The wear scar of the pin after the test at elevated temperature shows more elongated oxide layers (dark areas in Fig. 15b) originating from the top of unmelted tungsten particles than after the test at RT. These oxide layers consist probably of CoO, Co₃O₄, and Cr₂O₃ as identified in Ref. [24] by the Raman spectroscopy. Signs of strong plastic deformation are shown in Fig. 15c.

3.4 Hardfacing on ring-shaped component

To demonstrate the stability of the CMT hardfacing process using Stellite cored wire in longer-term cladding operation and functionality of weaving mode welding with a wide weave width on a circle, a ring-shaped component was hardfaced. As shown in Fig. 16, the process was capable of surfacing such a component with two adjacent beads overlapped with each other. The 3D image was scanned with a Hexagon HP-L-20.8 3D laser scanner (Hexagon Manufacturing Intelligence, Cobham, UK) and analyzed with Polyworks 2017 software (InnovMetric Software Inc., Quebec, Canada). In the analysis, the CAD model and the clad part were first aligned and then the difference between them was analyzed to obtain clad thicknesses. Thicknesses in as-clad conditions varied between 2.6 and 4.2 mm depending on the location. The cross-section image shows that two adjacent beads were smoothly joined together without any inter-run defects due

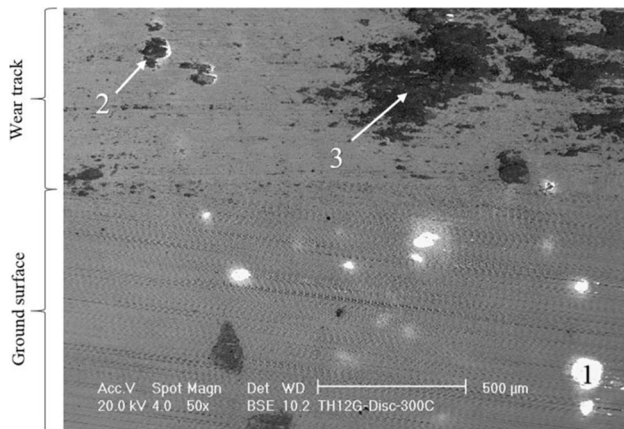


Fig. 14 BSE SEM micrograph showing the characteristic morphologies of non-tested ground surface and wear scar of CMT clad St12 disc after the test at 300 °C

Fig. 15 SEM images taken from the wear scar of CMT clad St12 a disc and b, c pin after test at 300 °C

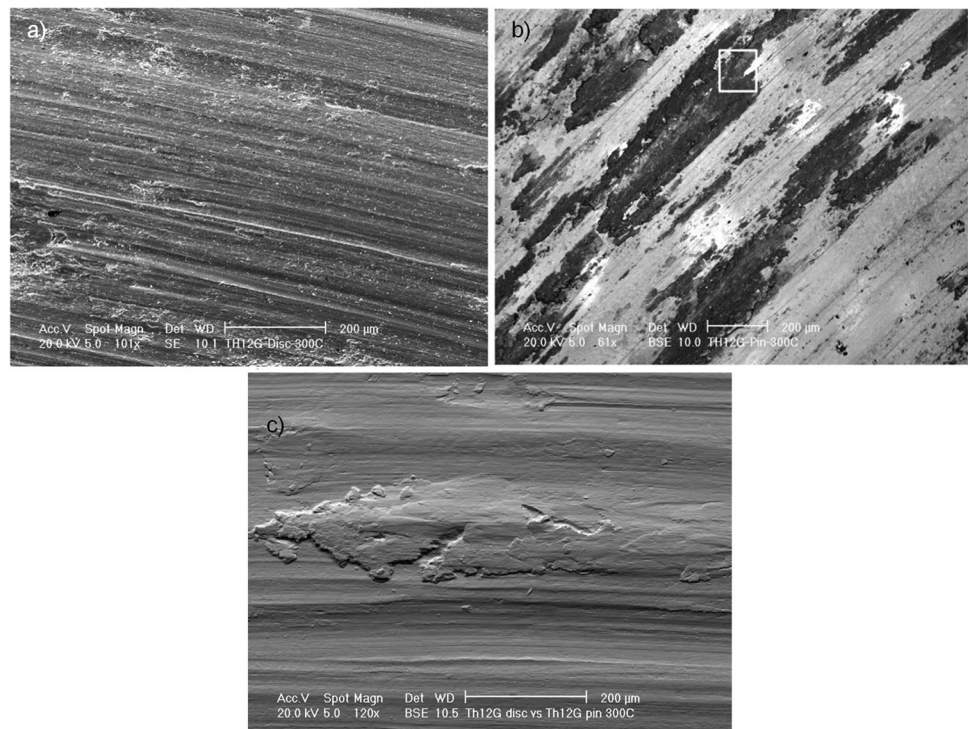
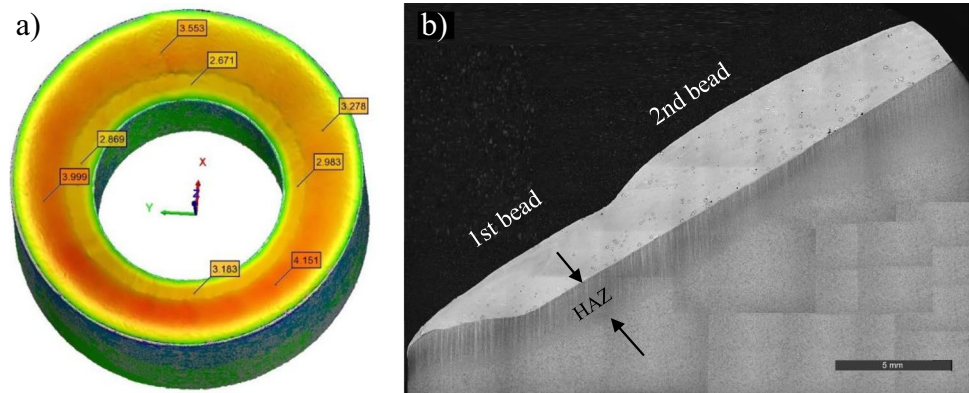


Fig. 16 CMT hardfaced ring-shaped component: **a** scanned 3D image showing clad thicknesses in millimeters and **b** cross-section of clad



to favorable contact angle. It is also seen that the fusion line is very straight indicating low penetration and dilution. The clad layer is, however, rather inhomogeneous due to insufficient melting of filler particles (W, Cr) inside the cored wire.

4 Conclusions

The objective of this study was to examine if CMT cladding is suitable for producing low diluted, fusion bonded, and defect-free single-layer hardfacings on martensitic stainless steel with a cored Stellite 12 filler wire and test their performance in self-mated sliding wear tests.

CMT cladding in a weaving mode can produce low diluted (< 5%) rather thick single-layer hardfacings (> 2.5 mm) with relatively high deposition rates (~ 3 kg/h) and hardness of ~490HV₁. The microstructure of the clad layer is characterized by large chromium and tungsten particles, which do not melt during welding leading to inhomogeneous coating structure, reduced clad hardness, and theoretically diminished ability to work harden.

In the self-mating sliding wear tests, it was noted that CMT hardfaced St12 did not reach the wear performance of self-mated laser clad Stellite 6, which in principle is a less alloyed and softer material than the grade St12. The Co-alloy from the counterpart adhered strongly to the unmelted tungsten particles both at RT and 300 °C.

To manufacture more homogeneous and harder clads, the size of the high melting point alloying elements inside the wire needs to be reduced. The size reduction of these particles would presumably raise the hardness of the clad and improve the wear resistance.

Acknowledgements This research was carried out as part of the ‘CMT – Nordic business opportunities from coating and additive manufacturing’ project which belonged to the European Interreg North 2014-2020 programme.

Funding The work has been made possible by financial support from European Regional Development Fund, Regional Council of Lapland,

Länsstyrelsen Norbotten, Kokkolan Seudun Kehitys Ltd., Wärtsilä Finland Oy, Rolls-Royce Oy Ab, Kokkola LCC Ltd., Ab A. Häggblom Oy, and Alfamat Oy.

Declarations

Conflict of interest The authors declare no competing interests.

Open Access This article is licensed under a Creative Commons Attribution 4.0 International License, which permits use, sharing, adaptation, distribution and reproduction in any medium or format, as long as you give appropriate credit to the original author(s) and the source, provide a link to the Creative Commons licence, and indicate if changes were made. The images or other third party material in this article are included in the article's Creative Commons licence, unless indicated otherwise in a credit line to the material. If material is not included in the article's Creative Commons licence and your intended use is not permitted by statutory regulation or exceeds the permitted use, you will need to obtain permission directly from the copyright holder. To view a copy of this licence, visit <http://creativecommons.org/licenses/by/4.0/>.

References

1. Davis JR. Surface engineering for corrosion and wear resistance. Maney Publ. 2001; 1–32
2. Mellor BG, Wood RJK, Jennett NM, et al. Surface coatings for protection against wear. Mellor BG, editor. Surf. Coatings Prot. Against Wear. Cambridge, England: Woodhead Publishing and Maney Publishing; 2006.
3. Lorenzin G, Rutili G (2009) The innovative use of low heat input in welding: experiences on ‘cladding’ and brazing using the CMT process. Weld Int 23:622–632. <https://doi.org/10.1080/09507110802543252>
4. Fronius. Cold Metal Transfer. 2014;16 Available from: http://www.fronius.com/cps/rde/xchg/SID-B0C6E4CC-0B1EFADC/fronius_international/hs.xsl/79_23609_ENG_HTML.htm#.U8Kn-bHwoJj.
5. Egerland SA (2009) Status and perspectives in overlaying under particular consideration of sophisticated welding processes. Q J Japan Weld Soc 27:50–54. <https://doi.org/10.2207/qjwjs.27.50s>
6. Ola OT, Doern FE (2014) A study of cold metal transfer clads in nickel-base INCONEL 718 superalloy. Mater Des 57:51–59. <https://doi.org/10.1016/j.matdes.2013.12.060>
7. Pickin CG, Williams SW, Lunt M (2011) Characterisation of the cold metal transfer (CMT) process and its application for low

- dilution cladding. *J Mater Process Tech* 211:496–502. <https://doi.org/10.1016/j.jmatprotec.2010.11.005>
8. Rajeev GP, Kamaraj M, Bakshi SR (2014) Al-Si-Mn alloy coating on aluminum substrate using cold metal transfer (CMT) welding technique. *JOM* 66:1061–1067. <https://doi.org/10.1007/s11837-014-0970-7>
 9. Rozmus-Górnikowska M, Cieniek L, Blicharski M et al (2014) Microstructure and microsegregation of an Inconel 625 weld overlay produced on steel pipes by the cold metal transfer technique. *Arch Metall Mater* 59:1081–1084. <https://doi.org/10.2478/amm-2014-0185>
 10. Zhang H, Hu S, Wang Z et al (2015) The effect of welding speed on microstructures of cold metal transfer deposited AZ31 magnesium alloy clad. *Mater Des* 86:894–901. <https://doi.org/10.1016/j.matdes.2015.07.143>
 11. Dutra JC, Silva RHG, Marques C et al (2016) A new approach for MIG/MAG cladding with Inconel 625. *Weld World* 60:1201–1209. <https://doi.org/10.1007/s40194-016-0371-3>
 12. Näkki J (2018) Properties of alloy 625 claddings made with laser and CMT methods. Dissertation. Tampere University of Technology
 13. Rajeev GP, Kamaraj M, Bakshi SR (2017) Hardfacing of AISI H13 tool steel with Stellite 21 alloy using cold metal transfer welding process. *Surf Coatings Technol* 326:63–71. <https://doi.org/10.1016/j.surfcoat.2017.07.050>
 14. Crook P. Cobalt and Cobalt Alloys. *ASM Handbook Vol. 2. Properties and selection: nonferrous alloys and special-purpose materials*. ASM International; 1990, 446–454
 15. Atamert S, Stekly J (1993) Microstructure, wear resistance and stability of cobalt based and alternative Iron based hardfacing alloys. *Surf Eng* 9:231–240. <https://doi.org/10.1179/sur.1993.9.3.231>
 16. Otterloo DMV, JL, De Hosson JTHM, (1997) Microstructural features and mechanical properties of a cobalt-based laser coating. *Acta mater* 45:1225–1236. [https://doi.org/10.1016/S1359-6454\(96\)00250-9](https://doi.org/10.1016/S1359-6454(96)00250-9)
 17. Kapoor S (2012) High-temperature hardness and wear resistance of Stellite alloys. Carleton University, Ottawa, Ontario
 18. Gilbert N. Stellite alloys – chemical composition, mechanical properties and common applications. <https://www.amazon.com/article.aspx?ArticleID=9857>
 19. Kapoor S, Liu R, Wu XJ et al (2012) Temperature-dependence of hardness and wear resistance of Stellite alloys. *World Acad Sci Eng Technol* 67:964–973. <https://doi.org/10.5281/zenodo.1060872>
 20. Yaedu AE, D'Oliveira ASCM (2005) Cobalt based alloy PTA hardfacing on different substrate steels. *Mater Sci Technol* 21:459–466. <https://doi.org/10.1179/174328413X13789824293380>
 21. Frenk A, Kurz W (1994) Microstructural effects on the sliding wear resistance of a cobalt-based alloy. *Wear* 174:81–91. [https://doi.org/10.1016/0043-1648\(94\)90089-2](https://doi.org/10.1016/0043-1648(94)90089-2)
 22. Fouillard L, El MM, Massaqa A (2009) Friction-induced work hardening of cobalt-base hardfacing deposits for hot forging tools. *J Mater Process Technol* 209:3366–3373. <https://doi.org/10.1016/j.jmatprotec.2008.07.039>
 23. Fouillard L, El Mansori M, Gerland M (2007) Role of welding process energy on the microstructural variations in a cobalt base superalloy hardfacing. *Surf Coatings Technol* 201:6445–6451. <https://doi.org/10.1016/j.surfcoat.2006.12.020>
 24. Motallebzadeh A, Atar E, Cimenoglu H (2015) Sliding wear characteristics of molybdenum containing Stellite 12 coating at elevated temperatures. *Tribol Int* 91:40–47. <https://doi.org/10.1016/j.triboint.2015.06.006>
 25. Kennametal Stellite. Stellite 12 alloy datasheet. Available from: http://www.stellite.com/Portals/0/KMT_Stellite12_DataSheet_FINAL.pdf
 26. Guest SD (2014) Depositing Ni-WC wear resistant overlays with hot-wire assist technology. Dissertation. University of Alberta
 27. ASTM G99–95a (2000) Standard test method for wear testing with a pin-on-disk apparatus.:417–421
 28. Atamert S, Bhadeshia HKDH (1989) Comparison of microstructures and abrasive wear properties of Stellite hardfacing alloys deposited by arc welding and laser cladding. *Metall Trans A* 20:1037–1053. <https://doi.org/10.1007/BF02650140>
 29. Hou QY, Gao JS, Zhou F (2005) Microstructure and wear characteristics of cobalt-based alloy deposited by plasma transferred arc weld surfacing. *Surf Coatings Technol* 194:238–243. <https://doi.org/10.1016/j.surfcoat.2004.07.065>
 30. Deloro Stellite. Stellite 12 alloy datasheet. Available from: www.deloro.com
 31. Deloro Stellite. Stellite 6 alloy datasheet. Available from: www.deloro.com
 32. Renz A, Prakash B, Hardell J, Lehmann O (2018) High-temperature sliding wear behaviour of Stellite®12 and Tribaloy®T400. *Wear* 402–403:148–159. <https://doi.org/10.1016/j.wear.2018.02.013>
 33. Recover scrap chromium by pyrometallurgy process. 911 Metallurgist. Available from <https://www.911metallurgist.com>
 34. Ellingham diagrams. Available from <https://web.mit.edu>
 35. Kennedy FE, Lu Y, Baker I (2015) Contact temperatures and their influence on wear during pin-on-disk tribotesting. *Tribol Int* 82:534–542. <https://doi.org/10.1016/j.triboint.2013.10.022>

Publisher's Note Springer Nature remains neutral with regard to jurisdictional claims in published maps and institutional affiliations.